https://doi.org/10.3311/PPch.39484

Periodica Polytechnica Chemical Engineering, 69(2), pp. 219–233, 2025

Hydrothermal Synthesis and Photocatalytic Efficiency of Turmeric Leaves Biochar/TiO_2 Composite for Photooxidation of Congo Red Dye

Raveena Malkari Katika[1], Sumalatha Boddu[1*], Ramesh Naidu Mandapati[1]

[1] Department of Chemical Engineering, Vignan's Foundation for Science, Technology & Research (Deemed to be University), Vadlamudi, 522213 Guntur, Andhra Pradesh, India
[*] Corresponding author, e-mail: drbsl_chem@vignan.ac.in

Received: 04 December 2024, Accepted: 16 April 2025, Published online: 15 May 2025

Abstract

The hydrothermal synthesis of an eco-friendly photocatalyst using turmeric leaves biochar (TLB) and titanium dioxide nanoparticle composite has been reported for the degradation of Congo Red (CR) dye. The synthesized composite was characterized using various analytical techniques, including X-ray diffraction (XRD), scanning electron microscopy (SEM), Brunauer-Emmett-Teller (BET) analysis, Fourier-transform infrared spectroscopy (FTIR) and X-ray photoelectron spectroscopy (XPS), confirming its structural and morphological attributes that ensured the uniform dispersion and intimate contact between TLB and TiO_2 particles. The degradation performance of the TLB/TiO_2 composite was examined by using UV light irradiation as a catalyst. The results demonstrated that the TLB/TiO_2 composite exhibited superior photocatalytic activity compared to pristine TiO_2, attributed to the enhanced light absorption, improved charge separation, and increased surface area provided by the biochar. The degradation kinetics followed a pseudo-first-order model, with a significant reduction in the dye concentration within a short time frame. The eco-friendly nature, cost-effectiveness, and high photocatalytic efficiency of the TLB/TiO_2 composite highlight its potential application in wastewater treatment, thus providing a novel approach to valorize agricultural waste into functional materials for sustainable environmental technologies.

Keywords

photocatalysis, turmeric leaves, hydrothermal method, Congo Red, TiO_2

1 Introduction

Water is a vital natural resource essential for the functioning of the planet. Ensuring the availability of clean and safe drinking water is crucial for maintaining optimal health and wellness. The accelerated pace of industrialization in recent decades has had a profound negative impact on the environment, particularly with respect to water quality. Industrial processes generate a diverse array of pollutants, including microbes, pesticides, heavy metals, pharmaceutical residues, and dyes, which are often released into water bodies, posing significant risks to both land and aquatic ecosystems [1–4]. The increasing contamination of water bodies by synthetic dyes, such as Congo Red (CR), a diazo dye possesses a characteristic azo group (–N=N–) within their molecular structure, contributing to their notable stability and poses a crucial environmental and health hazard due to their pathogenic, carcinogenic and non-biodegradable nature. Traditional methods for dye removal, including coagulation, adsorption, and biochemical treatments, result in low efficiency and possess high operating costs [5].

In this context, advanced oxidation processes (AOPs) have transformed as a superior method for eliminating organic pollutants in wastewater. These processes generate highly reactive oxidant radicals, primarily hydroxyl radicals, owing to its potential for complete mineralization under mild conditions [6, 7]. Photocatalysis stands out among AOPs due to its exceptional performance. This method relies on the activation of semiconductor catalysts through irradiation with UV or solar light. Among these semiconductors, TiO_2 is widely recognized as the most effective and cost-efficient photocatalyst for its exceptional photo reactivity, chemical stability, abundant availability, enviro-friendly, low cost, and strong oxidative power [8–10]. However, its practical application is constrained by low quantum efficiency, short-wavelength excitation, a wide bandgap, and the rapid recombination

Cite this article as: Malkari Katika, R., Boddu, S., Mandapati, R. N. "Hydrothermal Synthesis and Photocatalytic Efficiency of Turmeric Leaves Biochar/TiO_2 Composite for Photooxidation of Congo Red Dye", Periodica Polytechnica Chemical Engineering, 69(2), pp. 219–233, 2025.
https://doi.org/10.3311/PPch.39484

of photoinduced electron-hole pairs, all of which diminish its photocatalytic efficiency under visible light [11–13]. Various strategies have been investigated to overcome the limitations of TiO_2 photocatalysis, including the assimilation of metal or non-metal ions into the TiO_2 lattice, dye sensitization, and the application of noble metals on the TiO_2 surface. However, doping TiO_2 with metal ions frequently results in increased costs, reduced thermal stability, and higher toxicity. On the other hand, non-metal doping can introduce structural defects and involve complex synthesis processes. Both doping methods can potentially compromise photocatalytic efficiency and reduce the longevity of the material [14–16].

Recent research has focused on the development of TiO_2-based composites to enhance photocatalytic performance. Biochar, a carbon-rich material derived from the thermal conversion of waste biomass, offers a sustainable and eco-friendly additive for photocatalysts. The incorporation of biochar into TiO_2 not only improves light absorption and charge separation but also increases the surface area, and has rich oxygen-contained surface functional groups that provide additional active sites for photocatalytic reactions [17]. Consequently, a variety of plant-based biomass residues have been transformed into biochar, which subsequently served as a support material for TiO_2. For instance, Cai et al. [18] explored the adsorptive and photocatalytic efficiencies were assessed for the removal of Safranine T (ST) from an aqueous medium, under both UV-light irradiation and dark conditions by TiO_2 coated ramie bars biochar. Zhang and Lu [19] used coconut shell biochar as precursor to bound with TiO_2 *via* sol-gel method to remove Brilliant Blue dye. Li et al. [11] examined a catalyst based on N-doped chicken feather biochar coupled with TiO_2 for the visible-light-driven degradation of Rhodamine B [20]. Silvestri et al. [21] investigated the use of Salvinia molesta biochar coated with TiO_2 as a heterogeneous photocatalyst for the Acid Orange 7 dye decomposition. Lu et al. [22] decomposed methyl orange by sequence of TiO_2/walnut shell biochar synthesized *via* hydrolysis method. Shan et al. [23] degraded Methyl Orange by using biochar-coupled Ag and TiO_2 composites fabricated by photodeposition method. Brombilla et al. [24] investigated the detoriation of Rhodamine-B (RhB) dye using tea waste biochar that was enhanced with TiO_2 to function as a photocatalyst. Song et al. [25] studied the CR and Methylene Blue dye degradation using biochar integrated with H_3PO_4-TiO_2 nanoparticles. Kumar and Luxmi [26] reported agro-waste turmeric leaves as eco-friendly photo-catalyst. Although several biomasses have been used to create biochar for catalytic purposes, there has been no research on using turmeric leaves to create biochar for TiO_2 supports in photocatalysis.

Curcuma domestica (turmeric), a tropical crop grown vegetatively in Southeast Asia, has sparked attention in the medical, scientific, and culinary communities. Curcumin, the primary yellow pigment in turmeric (*Curcuma longa* L.), is widely utilized as a food ingredient, known for its medicinal properties in treating cancer, neurodegenerative diseases, rheumatoid arthritis, and cardiovascular conditions. However, after harvesting the turmeric roots, the foliage and stems are typically disposed of as waste. Further research is necessary to explore potential alternative uses for these residual plant materials. It exhibits strong absorption in the 420–580 nm visible light range due to its chemical and thermal stability, enhancing light absorption and inhibiting electron-hole recombination. Curcumin's molecular structure, characterized by two phenolic groups and two α, β-unsaturated carbonyl groups, allows for effective bonding to TiO_2 surfaces, making it ideal for photocatalytic degradation.

In this framework, the hydrothermal synthesis of turmeric leaves biochar (TLB)/TiO_2 nanocomposite and its utilization in the photo-oxidation of CR dye from aqueous medium is reported. The synthesized nanocomposite was characterized and operating parameters such as solution pH, UV irradiation period and catalyst concentration was studied for assessing its efficiency in degrading CR dye under UV light irradiation. Reusability evaluation of the catalyst was also carried out for its photocatalytic activity.

2 Materials and methods

2.1 Preparation of photo-catalyst

Biochar was synthesized through the thermal conversion of turmeric leaves procured from the campus of Vignan's Foundation for Science, Technology & Research (VFSTR), Guntur, India following the method described by Karimi et al. [27]. The turmeric leaves were washed with double-distilled water, air-dried, and ground using a ball mill to achieve particle size < 150 mesh. The crushed material was then pyrolyzed at 500 °C for 2 h in the presence of N_2 with a heating rate of 10 °C/min, producing the TLB sample. To engineer the biochar-TiO_2 composite (TLB/TiO_2), a simple hydrothermal method was employed using $TiCl_4$ as the precursor, to ensure uniform dispersion and intimate contact between biochar and TiO_2 nanoparticles. A dropwise addition of 10 mL $TiCl_4$ into 100 mL ultrapure water was performed, followed by the addition of biochar with constant

stirring maintaining the TLB/TiO_2 ratio as 2:1. The mixture was then enclosed in a Teflon-sealed autoclave at 200 °C for 2 h with a heating rate of 10 °C/min. The mixture was then cooled and centrifuged and the precipitate was collected. The obtained sample was oven dried, and calcined at 500 °C in a programmable muffle furnace for 2 h. The calcined samples were thoroughly pulverized using a mortar and pestle for further characterization. The resultant TLB/TiO_2 composite later used in photocatalytic assessment.

2.2 Characterization of photo-catalyst

The surface morphological analysis of TLB/TiO_2 composites was analyzed by scanning electron microscope (SEM) with an energy dispersive X-ray spectrometer (EDAX) (VEGA 3, SBH, TESCAN Brno S.R.O, Czech Republic) at magnification of 4.00 k. The X-ray diffraction (XRD) patterns of nano composites were recorded on X-ray diffractometer (Rigaku Miniflex 600, Rigaku Corporation, Japan) with Cu Kα radiation (λ = 0.1548 nm) at 40 kV and 80 mA in the region of 2θ from 10° to 80°. Infrared spectra of all samples were recorded using Fourier transform infrared spectrometer with diamond attenuated total reflection (FTIR-ATR) (Cary 630, Agilent Technologies, USA). The porous nature of the composite was determined by Brunauer-Emmett-Teller (BET) analysis using Belsorp Mini X Surface Area Analyzer (Microtrac MRB, Japan). X-ray photoelectron spectroscopy (XPS) was utilized to analyze the elemental composition and chemical states of the materials (K-Alpha, Thermo Scientific, UK). Diffuse reflectance spectra (DRS) were recorded using a UV-visible (UV-Vis) spectrometer (Cary 5000, Shimadzu, Japan) to determine the bandgap energy (E_g, eV). The optical absorption measurements were recorded by UV-Vis spectrophotometer (UV-2600, Shimadzu, Japan) in the range of 1200–200 nm.

2.3 Photodegradation essays

The photocatalytic activity of the TLB/TiO_2 composite was assessed for CR dye degradation under UV irradiation (16 W UV lamp, 353 nm) with magnetic stirring in a photoreactor. For the experiments, an appropriate amount of TLB/TiO_2 composite (0.1 to 0.5 g) was added to the dye solution (50 mL), followed by continuous stirring for 1 h in a dark environment to achieve adsorption-desorption equilibrium between the CR solution and the composite. The TLB/TiO_2 composite was able to adsorb 18% of CR dye [28, 29]. The suspension was then exposed to UV light in the reactor. To monitor the degradation process, 3 mL of dye-photocatalyst suspension were extracted at regular intervals during irradiation. These samples were centrifuged and analyzed by using a UV-visible spectrophotometer to measure absorbance at the CR dye's maximum wavelength (λ_{max} = 497 nm). The extent of degradation was determined by comparing the dye concentration before and after UV exposure. To optimize the degradation conditions, variables such as the amount of TLB/TiO_2 catalyst, irradiation time, initial CR concentration, and solution pH were systematically varied. The degradation ratio was obtained by the Eq. (1):

$$\mathrm{DR}(\%) = \frac{C_0 - C_t}{C_t} \times 100, \tag{1}$$

where C_0 is the initial concentration of CR, and C_t is the instant concentration in the sample with irradiation time (t) of CR dye solution, expressed in mg/L.

The kinetics of the photoinduced degradation process is assessed using Eq. (2):

$$\ln \frac{C_0}{C_t} = kt, \tag{2}$$

where k is the rate constant.

2.4 Scavenger study

Scavenger studies are integral for elucidating the mechanistic pathways of photocatalytic degradation, particularly in advanced materials like TLB/TiO_2 composites. In this study, the roles of reactive oxygen species (ROS) in the degradation process were probed using selective scavengers: triethanolamine (TEA) for photo- generated holes (h^+), 1,4-benzoquinone (BQ) for superoxide radicals $\left(\bullet O_2^-\right)$, isopropanol (IPA) for hydroxyl radicals (•OH) and potassium persulphate ($K_2S_2O_8$) for photo-generated electrons (e^-). Each scavenger was precisely dosed into the CR solution prior to catalyst introduction, enabling targeted quenching of the corresponding reactive species. All experiments were conducted under ambient conditions, providing insights into the relative contributions of these species to the overall photocatalytic activity.

3 Results and discussions

3.1 XRD analysis of TLB, TiO_2 and TLB/TiO_2

The XRD analysis of TLB, TiO_2, and the TLB/TiO_2 composite reveals key insights into their crystalline structures and phase compositions as shown in Fig. 1. The XRD pattern of TLB displays broad peaks, indicative of its predominantly amorphous structure, typical of TLB produced *via* pyrolysis. In contrast, TiO_2 and TLB/TiO_2 show sharp and

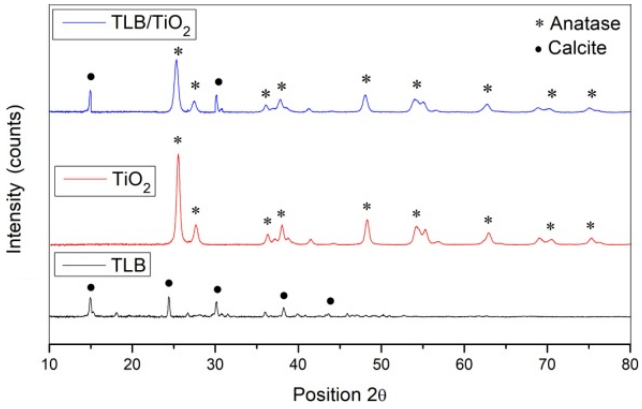

Fig. 1 XRD patterns of TLB, TiO_2 and TLB/TiO_2

well-defined peaks, at 2θ of 25.3°, 37.8°, 48.0°, 54.0°, 62.8°, 68.7°, 75.0°, and 82.5°, corresponding mainly to the anatase phase (JCPDS card no. 84-1286) confirming its high crystallinity [30, 31]. For the TLB/TiO_2 composite, the XRD pattern reflects the presence of both TLB and TiO_2. The characteristic TiO_2 peaks, particularly those of the anatase phase, are observed with reduced intensity, signifying successful incorporation of TiO_2 into the TLB matrix. This suggests that while the composite retains the amorphous nature of TLB, it also maintains the crystalline phases of TiO_2, indicating an effective interaction between the two components, which is critical for photocatalytic applications [21]. The Scherrer equation (Eq. (3)) yielded nanometer-sized crystallites, which optimize the rate of CR dye oxidation:

$$D = K\lambda/\beta\cos\theta, \tag{3}$$

where K is the Scherrer constant (taken as 0.89), λ is the incident wavelength of X-ray (0.154 nm), and β denotes the full width at half maximum of the peak. The typical size of the crystallite in the pure TiO_2 was found to be 25.58 nm, while the TLB/TiO_2 composite was found to be 35.47 nm, which leads to potential modifications in crystallinity. The interaction with TLB has contributed to controlled crystal growth, leading to enhanced surface properties and increased photocatalytic efficiency.

3.2 SEM-EDAX analysis of TLB, TiO_2 and TLB/TiO_2

The integrated SEM and EDAX provide detailed morphological and compositional analysis of TLB, TiO_2, and their composites. SEM imaging of TLB reveals its characteristic highly porous and irregular surface structure, which resulted from the pyrolysis of biomass. This porosity is critical to TLB's adsorption properties [21]. EDAX analysis of TLB primarily detects carbon, with possible traces of oxygen, potassium, and other elements that may vary depending on the source of biomass and pyrolysis conditions, as shown in Fig. 2. In contrast, SEM analysis of TiO_2 typically shows a fine, crystalline morphology with relatively uniform particle distribution, which can vary depending on its synthesis method and crystalline phase (anatase) [24]. EDAX of TiO_2 confirms its composition by identifying strong titanium and oxygen peaks, reflecting the material's high purity and concentration as shown in Fig. 3. When TLB is combined with TiO_2 to form a composite material, SEM images of TLB/TiO_2 composite illustrates that TiO_2 particles are dispersed across the TLB surface and are integrated within its pores. This dispersion is crucial, as it can influence the composite's functional properties, such as photocatalytic efficiency [26]. EDAX analysis of the composite shows a mix of elements from both the TLB and TiO_2 specifically carbon, titanium, and oxygen as shown in the Fig. 4. This compositional data provides insight into the distribution and interaction between the TiO_2 and the TLB matrix, which are critical factors in determining the composite's performance in applications like photocatalysis.

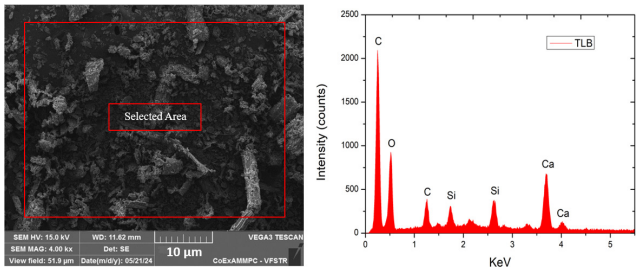

Fig. 2 EDAX analysis of TLB

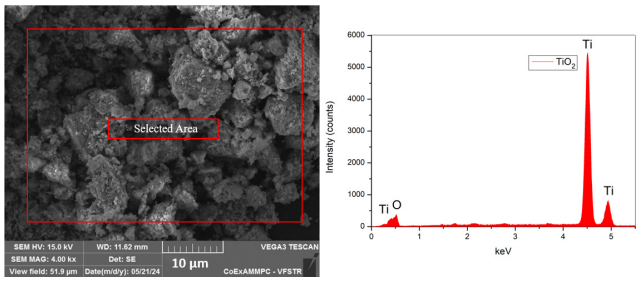

Fig. 3 EDAX analysis of TiO_2

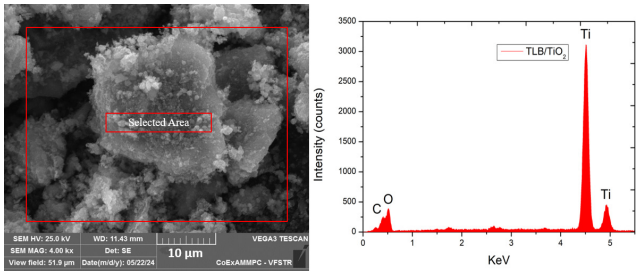

Fig. 4 EDAX analysis of TLB/TiO_2

3.3 FTIR analysis of TLB, TiO_2, TLB/TiO_2

The FTIR analysis of the TLB, TiO_2, and TLB/TiO_2 composite provides insight into the functional groups and interactions within these materials as shown in Fig. 5. The broad peak around 3400 1/cm in the TLB and TLB/TiO_2 spectra corresponds to O–H stretching, indicating the presence of hydroxyl groups, whereas TiO_2 alone shows a weaker signal, suggesting fewer hydroxyl functionalities. In TLB, CH_2 and CH_3 groups are identified by their characteristic stretching vibrations around 2929 1/cm indicating the presence of alkyl functional groups. Peaks around 2900–1700 1/cm in TLB and TLB/TiO_2 represent C–OH and C–O stretching, confirming the presence of organic functional groups [19, 32]. The peak near 1600 1/cm corresponds to C=C stretching, likely from aromatic rings or unsaturated hydrocarbons, and is prominent in TLB and TLB/TiO_2 [33, 34]. Additionally, a distinct C=O stretching vibration at approximately 1700 1/cm suggests the presence of carbonyl groups, such as ketones, esters, or carboxylic acids, primarily in TLB and TLB/TiO_2. The characteristic Ti–O stretching vibration appears in TiO_2 and TLB/TiO_2 at 600–800 1/cm [24], confirming the presence of TiO_2. Moreover, C–O–C and Si–O–Si stretching vibrations, observed around 1200 1/cm and 1100 1/cm respectively, indicate ether and siloxane functional groups in TLB. The peaks at 900–1000 1/cm correspond to C–C stretching, mainly seen in the TLB spectrum [24, 35]. These shifts and the combination of functional groups suggest strong interactions between the TLB matrix and TiO_2, reflecting the formation of a stable composite material. This composite structure could lead to improved properties, making it suitable for various applications, such as photocatalysis or pollutant adsorption [36, 37].

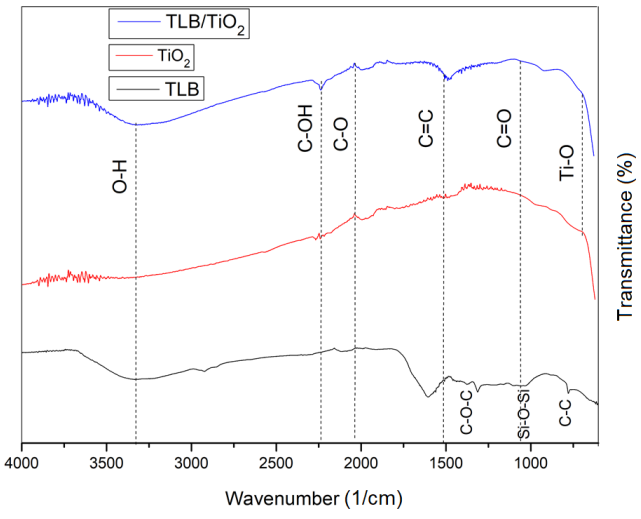

Fig. 5 FTIR of TLB, TiO_2 and TLB/TiO_2

3.4 XPS analysis of TLB, TiO_2, TLB/TiO_2

The XPS survey spectrum of the samples TLB, TLB/TiO_2 composite is depicted in Fig. 6 (a) and (b) revealed key insights into its oxidation states, coupling constant of energy levels, and chemical composition of the elements involved in the preparation of nano composites. Peaks corresponding to binding energies of core electrons indicate the presence of elements such as carbon, oxygen, and titanium without any additional noticeable peaks, suggesting the high purity of the composite. The XPS spectrum of Ti 2p shows strong peaks around 458–464 eV which are attributed to Ti $2p_{3/2}$ and Ti $2p_{1/2}$ energy levels, confirming the presence of TiO_2 in the composite. The binding energies and peak shapes provided information on the oxidation state of titanium, which are likely Ti^{+4} in TiO_2 [38]. The core-level XPS spectrum of Ti 2p is shown in Fig. 6 (c). The core-level C 1s XPS spectrum of the TLB/TiO_2 composite depicted in Fig. 6 (d) shows a prominent peak at 284.8 eV, indicating sp^2-hybridized carbon (C–C, C–H bonds) typical of aromatic structures, likely representing the biochar's carbon backbone. The broad, asymmetric peak suggests additional carbon groups like C–O, C=O, or O–C=O, implying that the biochar retains some of its original structure, potentially influencing the composite's surface chemistry and functionality. The core-level O1s XPS spectrum for the TLB/TiO_2 composite depicted in Fig. 6 (e) primarily shows a dominant peak centered around 530 eV, which corresponds to oxygen atoms in the TiO_2 lattice, indicating Ti–O bonds typical of TiO_2 [39]. A secondary peak around 532–534 eV is present, which suggests contributions from oxygen species not from the part of TiO_2 lattice, such as surface hydroxyl groups, adsorbed water, or carbon-oxygen bonds (C–O, C=O) from the biochar component. These higher binding energies of oxygen species point to the presence of surface oxidation and adsorption of oxygen-containing groups on both biochar and TiO_2. The composite's surface appears to have a mix of TiO_2 lattice oxygen and biochar-derived oxygen functionalities [40]. Thus, the spectrum indicates that the composite retains the distinct characteristics of TiO_2 alongside oxygenated functional groups from biochar, which enhances the composite's surface properties and reactivity. Overall, the XPS spectrum confirms the successful integration of biochar with TiO_2, suggesting potential applications in areas like photocatalysis.

3.5 Morphology of the surface of TLB, TiO_2 and TLB/TiO_2

The BET analysis of TLB/TiO_2 composites reveals critical surface characteristics, including distinct surface area, pore

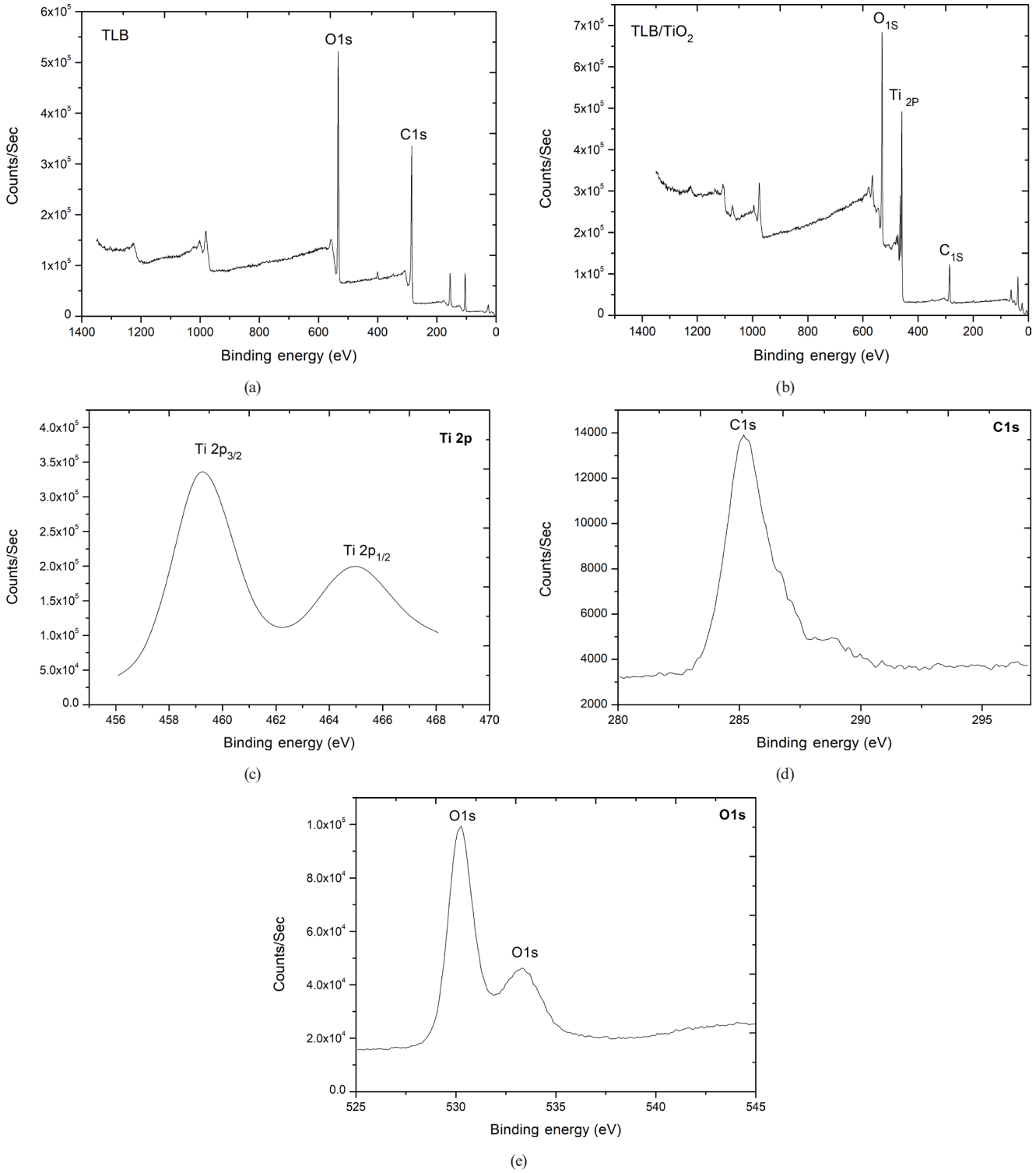

Fig. 6 (a) XPS survey spectrum of TLB; (b) XPS survey spectrum of TLB/TiO_2 composite; (c) Core level XPS spectrum of Ti 2p; (d) Core level XPS spectrum of O 1s; (e) Core level XPS spectrum of C 1s

volume, and pore size distribution, through N_2 adsorption measurements at varying pressures (Fig. 7). Table 1 presents the specific surface area, pore size distribution, and average pore diameter for TLB, TiO_2 and TLB/TiO_2 composite. The adsorption-desorption isotherm of TLB/TiO_2 exhibits a Type IV and H_3 hysteresis loop according to the IUPAC classification [41]. It is apparent that the composite's specific surface area is significantly greater than that of pure TiO_2 [42]. This growth in surface area and porous nature in the composite is attributed to the inherent structure of

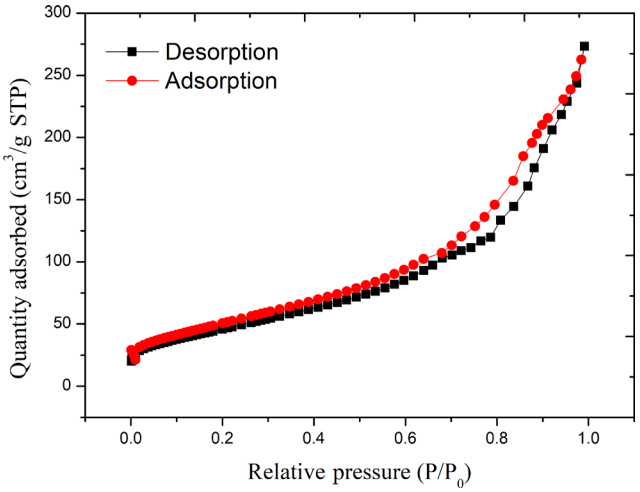

Fig. 7 Adsorption-desorption isotherm of TLB/TiO_2

Table 1 Pore properties of TLB, TiO_2 and TLB/TiO_2 composite

Sample	Surface area (m^2/g)	Pore volume (cm^3/g)	Pore size (Å)
TLB	73	0.0085	155
TiO_2	52	0.356	28
TLB/TiO_2	66	0.075	450

TLB and the nanoscale dispersion of TiO_2 particles, which enhance the contact area within catalytic systems [24, 43]. These properties are pivotal for applications that require enhanced photocatalytic efficiency, such as in water treatment. The BET analysis thus provides essential data for optimizing the TLB/TiO_2 ratio to achieve the desired performance characteristics.

3.6 UV-DRS analysis of TLB, TiO_2, TLB/TiO_2

The emission spectra of the UV source is shown in the Fig. 8 (a). The UV-DRS graph compares the optical properties of TiO_2, TLB, and the TLB/TiO_2 composite as shown in the Fig. 8 to calculate the bandgap energy (E_g, eV) using the Kubelka-Munk function:

$$F(R) = (1-R)^2 / 2R, \tag{4}$$

where R is the reflectance.

Equation (4) being defined by extending the linear part of a curve until it intersects the x-axis. The black curve from the graph representing pristine TiO_2 exhibited a band gap of 3.2 eV, consistent with its typical behavior as a wide band gap semiconductor, primarily absorbing in the UV region. The TLB showed a significantly lower band gap of 3.15 eV, indicating it can absorb light, likely due to the existence of carbonaceous structures and functional groups in the biochar. The TLB/TiO_2 composite presents an intermediate band gap of 2.86 eV, showing that the combination of

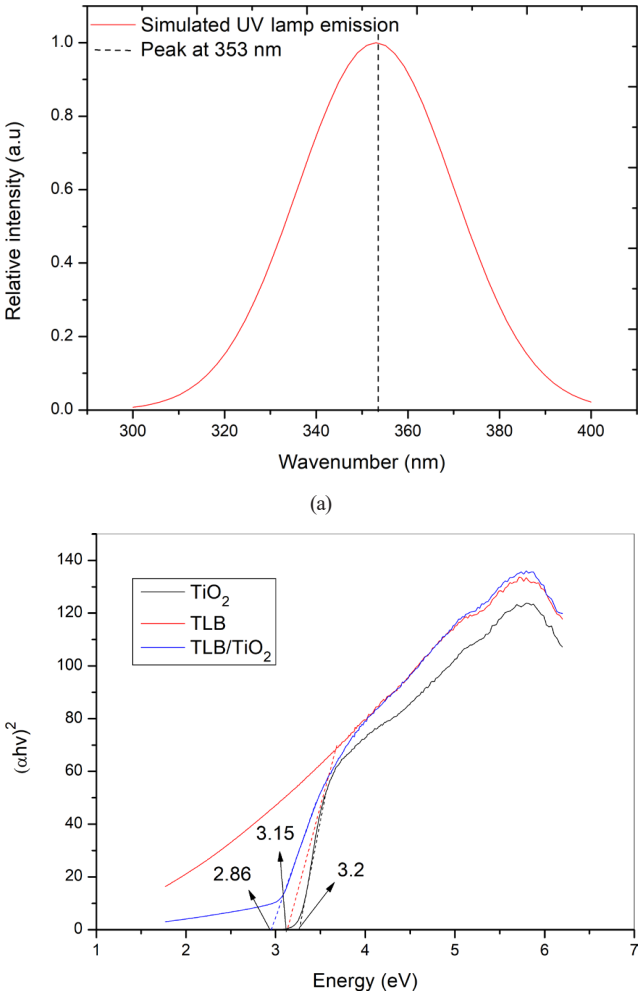

Fig. 8 (a) Emission spectra of the UV source; (b) UV-DRS graph of TLB, TiO_2 and TLB/TiO_2 with band gaps

TLB with TiO_2 shifts the absorption edge into the visible region. The reduction in band gap for the TLB/TiO_2 composite suggests that the integration of biochar with TiO_2 leads to improved charge transfer processes and enhanced electronic interaction between the two materials [21, 24]. This could reduce the recombination rate of charge carriers, thereby increasing the photocatalytic efficiency. Additionally, the modified electronic structure may enhance the material's response to a wider range of energies, making it potentially useful in applications such as water splitting, pollutant degradation, or other catalytic processes where efficient light absorption and charge separation are critical.

3.7 Wetting properties of TLB, TiO_2, TLB/TiO_2

The wetting properties and aqueous stability of TL biochar, TiO_2, and the TLB/TiO_2 composite were evaluated using a goniometer for contact angle measurements and dispersion

stability tests (Lb-10CAG, Labotronics Scientific, USA). TL biochar, being carbonaceous, exhibited moderate hydrophobicity, while TiO_2 demonstrated superhydrophilicity. The TLB/TiO_2 composite showed improved hydrophilicity compared to TLB due to the incorporation of TiO_2, enhancing water interaction. Dispersion stability tests in deionized water revealed that TL biochar settled over time, while TiO_2 exhibited some agglomeration. However, the TLB/TiO_2 composite remained well-dispersed, indicating better aqueous stability as shown in the Fig. 9. These findings suggest that TLB/TiO_2 has superior wetting properties and dispersion, making it highly suitable for photocatalytic applications in water treatment. The enhanced hydrophilicity of the composite ensures better interaction with waterborne pollutants, facilitating efficient photocatalytic degradation. Additionally, the improved dispersion stability minimizes the catalyst loss and enhances reusability, further contributing to its practical applicability in environmental remediation [44].

3.8 Photocatalytic performance of TLB/TiO_2

The photocatalytic degradation process of organic impurities, such as azo dyes, by nanocomposites can be summarized in Eqs. (5) to (13), where CB is the conduction band, and VB is the valence band. Upon photo irradiation, nano-photocatalysts become excited, generating electrons and holes. These electrons ionize the adsorbed oxygen, forming superoxide free radical anions. Concurrently, water ionizes into hydroxide anions and hydrogen cations. The hydroxide ions are oxidized by holes (h^+) to form hydroxyl radicals, while superoxide radical anions are propagated by the formed hydrogen cations to create peroxide radicals [27]. Peroxide radicals co-scavenge electrons to produce hydroperoxide anions, which subsequently protonate to form hydrogen peroxide. This hydrogen peroxide further reacts with electrons to generate hydroxyl radicals and hydroxide anions as shown in Fig. 10. These active species participated in degrading the CR dye. Additionally, the effects of irradiation time, pH, catalyst dosage, and dye concentration were examined to observe the optimal conditions for the degradation of CR dye [31].

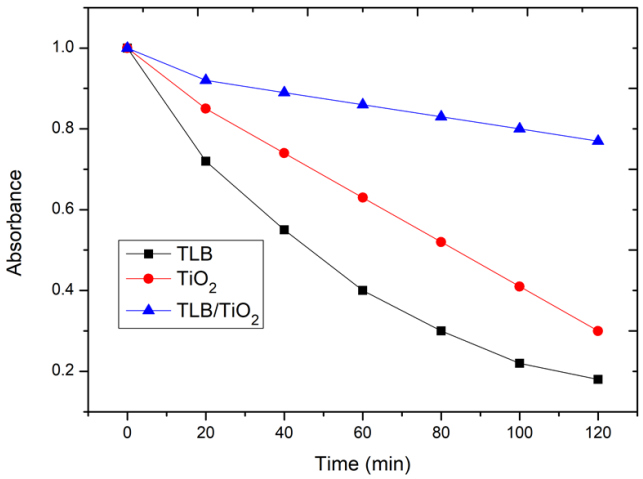

Fig. 9 Dispersion stability of TLB, TiO_2, TLB/TiO_2

$$\mathrm{TLB/TiO_2} + h\nu \rightarrow e^-_{CB} + h^+_{VB} \quad (5)$$

$$O_2 + e^- \rightarrow {}^{\bullet}O_2^- \quad (6)$$

$$H_2O \rightarrow HO^- + H^+ \quad (7)$$

$$HO^- + h^+ \rightarrow {}^{\bullet}HO \quad (8)$$

$${}^{\bullet}O_2^- + H^+ \rightarrow {}^{\bullet}HO_2 \quad (9)$$

$${}^{\bullet}HO_2 + e^- \rightarrow {}^{\bullet}HO_2^- \quad (10)$$

$${}^{\bullet}HO_{2-} + H^+ \rightarrow H_2O_2 \quad (11)$$

$$H_2O_2 + e^- \rightarrow {}^{\bullet}HO + HO^- \quad (12)$$

$$\text{CR dye} + \text{active species}\left({}^{\bullet}HO, h^+, e^-, {}^{\bullet}O_2^-\right) \rightarrow CO_2 + H_2O \quad (13)$$

The photocatalytic degradation of CR dye is anticipated to follow two primary pathways: the chromophore degradation pathway and the auxochrome degradation pathway. In the chromophore degradation pathway, ROS such as superoxide radicals $\left({}^{\bullet}O_2^-\right)$ and hydroxyl radicals (•OH) attack the chromophore, initiating the cleavage of azo bonds (–N=N–) and disrupting the aromatic rings, which breaks the conjugated system. In the auxochrome degradation pathway, hydroxyl radicals (•OH) oxidize the sulfonic acid (–SO_3H) and amine (–NH_2) groups, leading to their detachment from the dye molecule and conversion to sulfate ions $\left(SO_4^{2-}\right)$ and ammonia (NH_3), respectively. The simultaneous degradation of both chromophore and auxochrome groups ensures the comprehensive breakdown of CR dye [15, 31]. By disrupting both the color-imparting

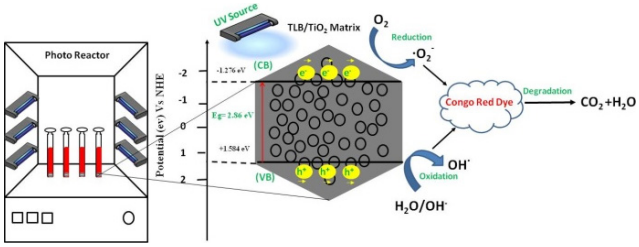

Fig. 10 Photocatalytic mechanism of CR dye degradation (NHE: normal hydrogen electrode, CB: conduction band, VB: valence band)

structures and the functional groups that influence dye properties, the TLB/TiO_2 composite efficiently degrades CR into harmless end-products such as CO_2, H_2O, and other small organic molecules. This dual-pathway degradation is critical for the effective photocatalytic treatment of dye-contaminated water.

3.8.1 Effect of irradiation time

The graph demonstrates the impact of contact time on the photodegradation efficiency of CR dye using TLB, TiO_2, and TLB/TiO_2 composite as shown in Fig. 11. The TLB alone exhibits a moderate degradation rate, reaching about 65% after 120 min, reflecting its limited photocatalytic activity. In contrast, TiO_2 shows a higher degradation efficiency of approximately 85% over the same period, consistent with its established photocatalytic properties. Notably, TLB/TiO_2 composite achieves the highest degradation efficiency, reaching around 95% within the first 60 min and maintaining this level thereafter. This superior performance is attributed to the synergistic interaction between TLB's adsorption capacity and TiO_2's photocatalytic activity, which likely enhances charge separation and light absorption [24, 27]. These results highlight the effectiveness of the TLB/TiO_2 composite in environmental remediation, particularly in the efficient degradation of azo dyes like CR.

3.8.2 Effect of pH

The graph demonstrates the contribution of pH on the degradation of CR dye using TLB, TiO_2, and TLB/TiO_2 composite as shown in Fig. 12. All materials show optimal degradation in acidic conditions, with the highest efficiency occurring at pH 4. TLB alone reaches around 60% degradation at this pH, while TiO_2 achieves approximately

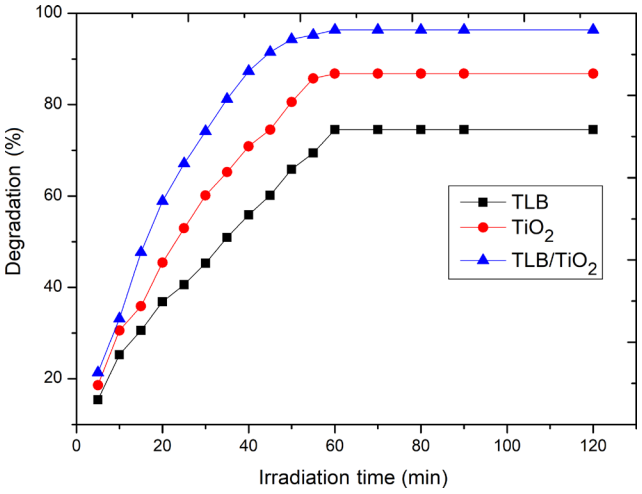

Fig. 11 Effect of irradiation time in case of TLB, TiO_2, and TLB/TiO_2

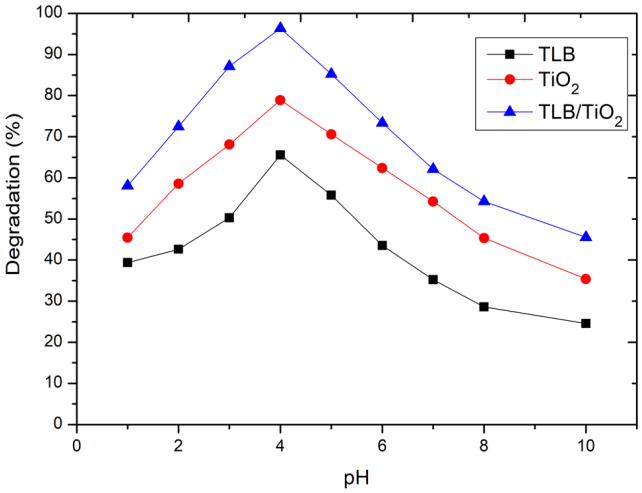

Fig. 12 Effect of pH of TLB, TiO_2 and TLB/TiO_2 suspensions

75%. The TLB/TiO_2 composite outperforms both, reaching nearly 95% degradation at pH 4 and maintaining superior efficiency across the entire pH range. The enhanced conduct of the composite can be associated to the synergistic effects of TLB's adsorption capacity and TiO_2's photocatalytic activity, which are particularly effective in acidic environments. The decline in degradation efficiency at higher pH levels is likely due to reduced proton availability and changes in the surface electrostatic charge of the materials, which negatively impact dye adsorption and subsequent photodegradation [21, 27]. These results underscore the significance of pH in optimizing the photocatalytic degradation of organic pollutants using composite materials like TLB/TiO_2.

3.8.3 Effect of catalyst concentration

The graph depicts the impact of various catalyst concentration on the photocatalytic degradation of CR dye by using TLB, TiO_2, and TLB/TiO_2 as shown in Fig. 13. The composite exhibits the highest activity, nearing 95% degradation at 50 mg and above, likely due to the enhanced charge separation and increased active sites from the combination of TLB and TiO_2. TiO_2 also shows strong performance, consistently achieving over 80% degradation, in line with its known photocatalytic properties. TLB, with the lowest efficiency, improves with increasing catalyst concentration, reaching around 70% at higher levels. Photocatalysis relies on light activation, and at optimal dosages, the catalyst's surface is efficiently exposed to light. However, as the dosage increases beyond the optimal level, the catalyst particles can scatter and absorb more light, leading to a shielding effect with increase in the turbidity of the solution, which in turn reduces the infusion of light into the solution [34, 35].

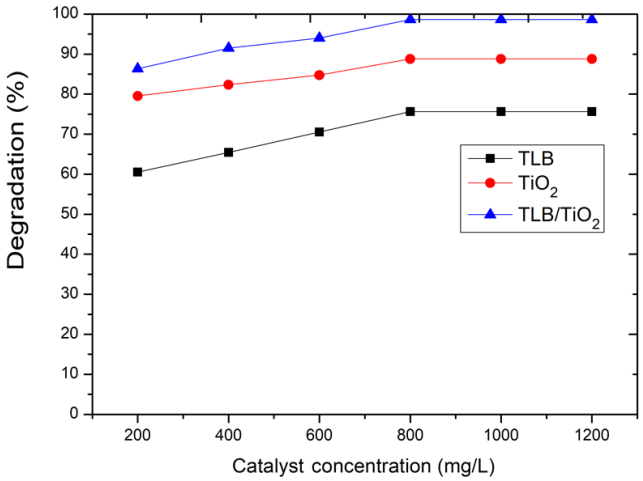

Fig. 13 Effect of TLB, TiO_2 and TLB/TiO_2 catalyst concentration

This limits the activation of catalyst particles throughout the solution, concentrating the photocatalytic activity near the surface and decreasing overall efficiency. TLB/TiO_2 composite significantly outperforms the other catalysts, making it the most effective for CR dye oxidation.

3.8.4 Effect of dye concentration

The graph illustrates that the photoinduced degradation efficiency of CR dye decreases as the initial dye concentration increases for all three catalysts: TLB, TiO_2, and TLB/TiO_2 as shown in Fig. 14. Among these, TLB/TiO_2 composite demonstrates the highest performance, achieving over 95% degradation at low concentrations (10 ppm) and maintaining around 75% efficiency at 60 ppm. TiO_2 follows a similar trend but with slightly lower efficiency, starting at 85% and stabilizing around 70%. TLB, primarily functioning as an adsorbent, shows the lowest degradation rates, dropping below 60% at higher concentrations. The decline

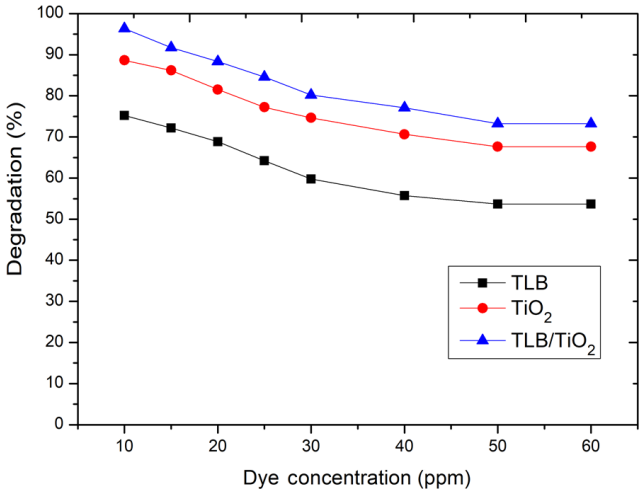

Fig. 14 Effect of dye concentration in case of TLB, TiO_2 and TLB/TiO_2

in photocatalytic degradation efficiency beyond the optimal dye concentration is due to several interconnected factors. First, the catalyst's active sites become saturated, limiting further adsorption and degradation. The increased dye concentration also leads to greater opacity in the solution, reducing light penetration and diminishing catalyst activation. Additionally, the higher concentration intensifies competition for the limited reactive species generated by the catalyst. The formation of intermediate by-products at elevated dye concentrations may further complicate the degradation process by competing for active sites. Lastly, mass transfer limitations arise as the concentration gradient increases, hindering the diffusion of dye molecules to the catalyst surface, which reduces overall contact and efficiency [21, 27, 34]. Overall, TLB/TiO_2 outperforms the other catalysts due to its superior photocatalytic properties, even at higher dye concentrations.

3.8.5 Degradation kinetics

The kinetic models, such as the pseudo-first-order and pseudo-second-order models, were used to analyze the degradation kinetics of CR dye by the TLB/TiO_2 composite, as shown in Fig. 15 (a) and (b), respectively. These models are typically employed to describe adsorption and degradation kinetics, where the concentration of CR over time is assessed. The first graph, which fits the data to the pseudo-first-order model, shows a strong linear relationship, indicating that the degradation of CR by the TLB/TiO_2 composite closely follows pseudo-first-order kinetics. The linearity suggests that the degradation rate primarily depends on the dye concentration. The second graph, fitting the pseudo-second-order model, shows some degree of linearity but with more noticeable deviations from the ideal trend. This implies that, while the pseudo-second-order model could also illustrate the kinetics, it is not as accurate as the pseudo-first-order model for this particular degradation process. The regression coefficient values support the conclusion that pseudo-first-order kinetics (with an R^2 value of 0.988) provides a much better fit for the degradation of CR by the TLB/TiO_2 composite than pseudo-second-order kinetics (with an R^2 value of 0.856) [24, 35]. The near-perfect fit suggests that the degradation of CR predominantly follows first- order kinetics, indicating that the degradation rate is directly proportional to the dye concentration. This further reinforces the idea that the reaction mechanism likely involves direct photolysis and simple catalytic breakdown without complex surface interactions.

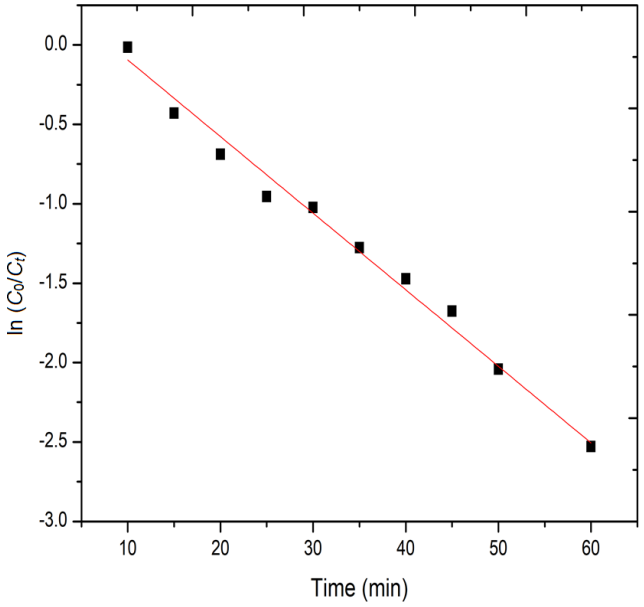

(a)

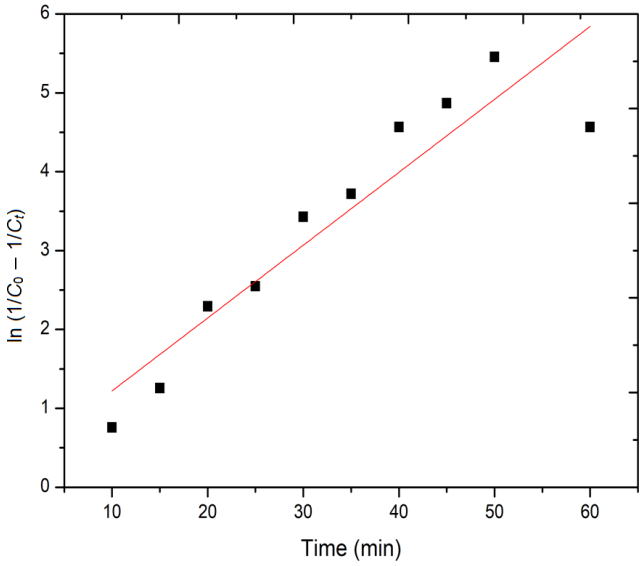

(b)

Fig. 15 (a) First order degradation kinetics with TLB/TiO_2; (b) Second order degradation kinetics with TLB/TiO_2

3.9 Effect of scavengers on degradation

The rate of photocatalytic degradation performance is directly impacted by the amount of photoinduced active radical species by ROS. Various radical species are engaged in the photodegradation of organic dyes, such as e^-, h^+, $^\bullet OH$, and $^\bullet O_2^-$. During tests, scavengers' sacrificial agents can be used to trap these radicals. The specific function of every radical is ascertained by means of a meticulous evaluation and refinement of reaction parameters. To target e^-, h^+, $^\bullet OH$, and $^\bullet O_2^-$, respectively, scavengers such as $K_2S_2O_8$, TEA, IPA, and p-BQ were used. Compared to $K_2S_2O_8$ and TEA, it was discovered that the rate inhibition

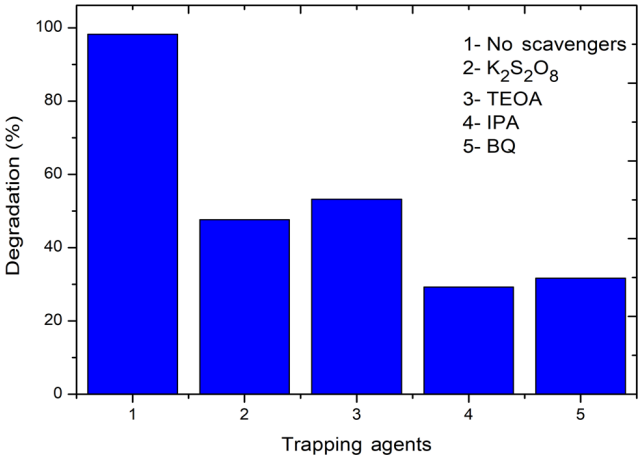

Fig. 16 Scavenger study with TLB/TiO_2 composite

effect was more noticeable with IPA and BQ. Fig. 16 depicts the decrease in CR dye degradation efficiency as a result of scavenging. $K_2S_2O_8$ and TEA, the other two scavengers, had a less noticeable impact on the photodegradation of CR dye. Thus, the scavenger study indicates that superoxide anions $\left(^\bullet O_2^-\right)$ and hydroxyl radicals ($^\bullet OH$) are important, but electrons (e^-) and holes (h^+) have little effect, as shown by the hydrogen peroxide's involvement in the photocatalytic destruction of CR dye [34, 35, 42].

3.10 Reusability and stability

To assess the stability and potential for reuse of the produced photocatalyst, its recyclability was evaluated. The catalyst was isolated by centrifugation and cleaned three times with ethyl alcohol and distilled water. Then it was dried for 6 h at 60 °C to prepare it for another cycle. As shown in Fig. 17 (a), the photocatalyst can be reused up to five cycles not having any substantial reduction in photocatalytic activity. However, nanocomposite degradation efficiency may decrease due to surface site blockage and changes in the porous structure. The stability of the TLB/TiO_2 photocatalyst is primarily attributed to the TLB component and effective charge separation. The photocatalyst exhibited an exemplary reusability by achieving a photodegradation effectiveness of 92.48% even after the five runs. Additionally, XRD analysis was carried out to confirm the material's stability after the first and fifth runs, as illustrated in Fig. 17 (b). The firmness of the TLB/TiO_2 photocatalyst was validated by the absence of crucial changes in the positions or intensities of the XRD peaks and retains same crystalline phase. To validate the adsorption of CR dye into the composite, functional groups of the photocatalyst were analyzed by using FTIR and the corresponding graph was depicted in Fig. 17 (c). When compare to the IR results of the composite before adsorption (as in Fig. 5) changes were observed around 1500–1600 1/cm

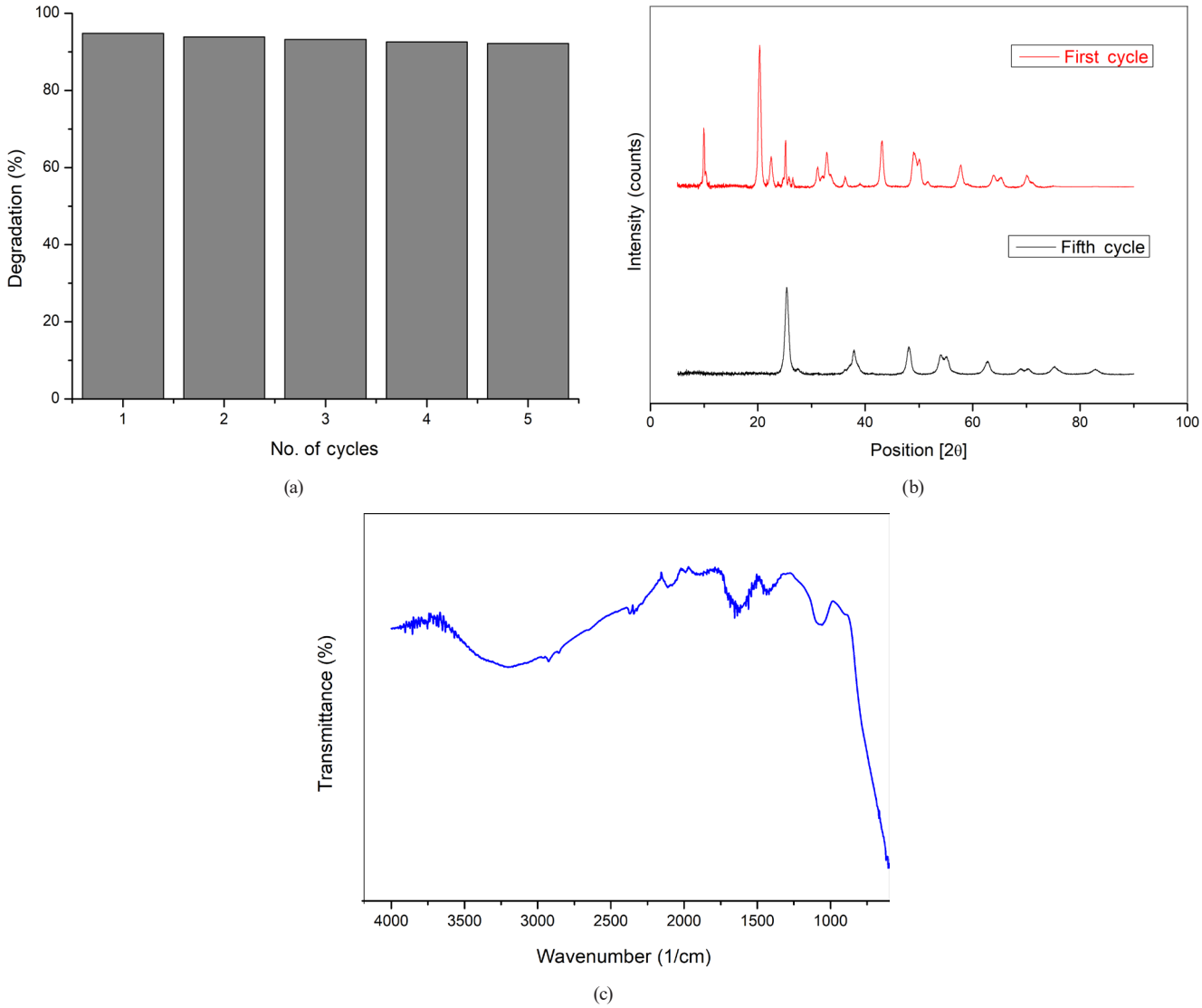

Fig. 17 (a) Reusability of TLB/TiO_2 composite over CR dye degradation; (b) XRD of TLB/TiO_2 composite after first and fifth cycle of CR dye degradation; (c) FTIR of TLB/TiO_2 composite after CR dye degradation

and 1000–1750 1/cm regions attributes to degradation products, while the stable Ti–O band (600–800 1/cm) confirms TiO_2's structural integrity.

4 Conclusions

The hydrothermal method effectively integrated the TLB with TiO_2 by creating a composite with enhanced photocatalytic properties. This composite demonstrates significant efficiency in the photooxidation of CR dye under UV light, showing a high degradation rate and excellent stability with lower bandgap energy of 2.86 eV. The photocatalytic performance of the TLB/TiO_2 composite is attributed to the synergistic effects of TLB's high surface area (66 m^2/g) and TiO_2's photocatalytic activity. The TLB enhances the adsorption of the dye, while TiO_2 generates ROS under UV irradiation, leading to the effective breakdown of CR dye into simpler molecules. The composite was balanced and effective after five cycles of reuse. The results highlight the potential of using natural, low-cost materials in AOPs for wastewater treatment. The composite demonstrates a sustainable and efficient solution for environmental remediation.

Acknowledgement

The Authors are thankful to the management of Vignan's Foundation for Science, Technology and Research, Guntur, Andhra Pradesh for the continuous support throughout the work.

The authors extend their sincere gratitude to Dr. Chandrasekar Kuppan, Professor in the Department of Chemistry at VFSTR, for his expertise and insights, which have been instrumental in shaping our research efforts and achieving significant progress in this project by using photo reactor.

References

[1] Benkhaya, S., M'rabet, S., El Harfi, A. "A review on classifications, recent synthesis and applications of textile dyes", Inorganic Chemistry Communications, 115, 107891, 2020. https://doi.org/10.1016/j.inoche.2020.107891

[2] Butburee, T., Bai, Y., Wang, L. "Unveiling general rules governing the dimensional evolution of branched TiO_2 and impacts on photoelectrochemical behaviors", Journal of Materials Chemistry A, 9(41), pp. 23313–23322, 2021. https://doi.org/10.1039/D1TA05218G

[3] Prajapati, A. K., Mondal, M. K. "Green synthesis of Fe_3O_4-onion peel biochar nanocomposites for adsorption of Cr(VI), methylene blue and congo red dye from aqueous solutions", Journal of Molecular Liquids, 349, 118161, 2022. https://doi.org/10.1016/j.molliq.2021.118161

[4] Samsami, S., Mohamadizaniani, M., Sarrafzadeh, M.-H., Rene, E. R., Firoozbahr, M. "Recent advances in the treatment of dye-containing wastewater from textile industries: Overview and perspectives", Process Safety and Environmental Protection, 143, pp. 138–163, 2020. https://doi.org/10.1016/j.psep.2020.05.034

[5] Weldegebrieal, G. K. "Synthesis method, antibacterial and photocatalytic activity of ZnO nanoparticles for azo dyes in wastewater treatment: A review", Inorganic Chemistry Communications, 120, 108140, 2020. https://doi.org/10.1016/j.inoche.2020.108140

[6] Wang, M., Li, J., Ning, S., Fu, X., Wang, X., Tan, L. "Simultaneously enhanced treatment efficiency of simulated hypersaline azo dye wastewater and membrane antifouling by a novel static magnetic field membrane bioreactor (SMFMBR)", Science of The Total Environment, 821, 153452, 2022. https://doi.org/10.1016/j.scitotenv.2022.153452

[7] Nakata, K., Fujishima, A. "TiO_2 photocatalysis: Design and applications", Journal of Photochemistry and Photobiology C: Photochemistry Reviews, 13(3), pp. 169–189, 2012. https://doi.org/10.1016/j.jphotochemrev.2012.06.001

[8] Chandrabose, G., Dey, A., Gaur, S. S., Pitchaimuthu, S., Jagadeesan, H., Braithwaite, N. S. J., Selvaraj, V., Kumar, V., Krishnamurthy, S. "Removal and degradation of mixed dye pollutants by integrated adsorption-photocatalysis technique using 2-D MoS_2/TiO_2 nanocomposite", Chemosphere, 279, 130467, 2021. https://doi.org/10.1016/j.chemosphere.2021.130467

[9] Zarei, N., Behnajady, M. A. "Synthesis, characterization, and photocatalytic activity of sol–gel prepared Mg/ZnO nanoparticles", Desalination and Water Treatment, 57(36), pp. 16855–16861, 2016. https://doi.org/10.1080/19443994.2015.1083479

[10] Khan, A. A., Mukherjee, S., Mondal, M., Boddu, S., Subbaiah, T., Halder, G. "Assessment of algal biomass towards removal of Cr(VI) from tannery effluent: a sustainable approach", Environmental Science and Pollution Research, 29(41), pp. 61856–61869, 2022. https://doi.org/10.1007/s11356-021-16102-8

[11] Li, Y., Cao, S., Zhang, A., Zhang, C., Qu, T., Zhao, Y., Chen, A. "Carbon and nitrogen co-doped bowl-like Au/TiO_2 nanostructures with tunable size for enhanced visible-light-driven photocatalysis", Applied Surface Science, 445, pp. 350–358, 2018. https://doi.org/10.1016/j.apsusc.2018.03.187

[12] Dulla, J. B., Sumalatha, B., Alugunulla, V. N., Tc, V. "Ultrasonic treated dried turmeric leaves powder as biosorbent for enhanced removal of lead from aqueous solutions", International Journal of Environmental Analytical Chemistry, 104(16), pp. 3723–3741, 2024. https://doi.org/10.1080/03067319.2022.2089566

[13] Zhang, S., Zhang, J., Sun, J., Tang, Z. "Capillary microphotoreactor packed with TiO_2-coated glass beads: An efficient tool for photocatalytic reaction", Chemical Engineering and Processing - Process Intensification, 147, 107746, 2020. https://doi.org/10.1016/j.cep.2019.107746

[14] Li, G., Park, S., Rittmann, B. E. "Developing an efficient TiO_2-coated biofilm carrier for intimate coupling of photocatalysis and biodegradation", Water Research, 46(19), pp. 6489–6496, 2012. https://doi.org/10.1016/j.watres.2012.09.029

[15] Silvestri, S., dos Santos Trentin, R., da Silveira Salla, J., Foletto, E. L. "Improved Photocatalytic Performance for Rhodamine B Degradation by Porous Zn_2SnO_4 Prepared with Carbon Black as a Pore-Forming Agent", Water, Air, & Soil Pollution, 230(8), 186, 2019. https://doi.org/10.1007/s11270-019-4239-1

[16] Das, S., Mahalingam, H. "Dye degradation studies using immobilized pristine and waste polystyrene-TiO2/rGO/g-C_3N_4 nanocomposite photocatalytic film in a novel airlift reactor under solar light", Journal of Environmental Chemical Engineering, 7(5), 103289, 2019. https://doi.org/10.1016/j.jece.2019.103289

[17] Gupta, A. D., Singh, H., Varjani, S., Awasthi, M. K., Giri, B. S., Pandey, A. "A critical review on biochar-based catalysts for the abatement of toxic pollutants from water via advanced oxidation processes (AOPs)", Science of the Total Environment, 849, 157831, 2022. https://doi.org/10.1016/j.scitotenv.2022.157831

[18] Cai, X., Li, J., Liu, Y., Yan, Z., Tan, X., Liu, S., Zeng, G., Gu, Y., Hu, X., Jiang, L. "Titanium dioxide-coated biochar composites as adsorptive and photocatalytic degradation materials for the removal of aqueous organic pollutants", Journal of Chemical Technology and Biotechnology, 93(3), pp. 783–791, 2018. https://doi.org/10.1002/jctb.5428

[19] Zhang, S., Lu, X. "Treatment of wastewater containing Reactive Brilliant Blue KN-R using TiO_2/BC composite as heterogeneous photocatalyst and adsorbent", Chemosphere, 206, pp. 777–783, 2018. https://doi.org/10.1016/j.chemosphere.2018.05.073

[20] Li, H., Hu, J., Zhou, X., Li, X., Wang, X. "An investigation of the biochar-based visible-light photocatalyst via a self-assembly strategy", Journal of Environmental Management, 217, pp. 175–182, 2018. https://doi.org/10.1016/j.jenvman.2018.03.083

[21] Silvestri, S., Gonçalves, M. G., da Silva Veiga, P. A., da Silva Matos, T. T., Peralta-Zamora, P., Mangrich, A. S. "TiO_2 supported on *Salvinia molesta* biochar for heterogeneous photocatalytic degradation of Acid Orange 7 dye", Journal of Environmental Chemical Engineering, 7(1), 102879, 2019. https://doi.org/10.1016/j.jece.2019.102879

[22] Lu, L., Shan, R., Shi, Y., Wang, S., Yuan, H. "A novel TiO_2/biochar composite catalysts for photocatalytic degradation of methyl orange", Chemosphere, 222, pp. 391–398, 2019. https://doi.org/10.1016/j.chemosphere.2019.01.132

[23] Shan, R., Lu, L., Gu, J., Zhang, Y., Yuan, H., Chen, Y., Luo, B. "Photocatalytic degradation of methyl orange by Ag/TiO_2/biochar composite catalysts in aqueous solutions", Materials Science in Semiconductor Processing, 114, 105088, 2020. https://doi.org/10.1016/j.mssp.2020.105088

[24] Brombilla, V. d. L., Sarmento Lazarotto, J., Silvestri, S., Anschau, K. F., Dotto, G. L., Foletto, E. L. "Biochar derived from yerba-mate (*Ilex paraguariensis*) as an alternative TiO_2 support for enhancement of photocatalytic activity toward Rhodamine-B degradation in water", Chemical Engineering Communications, 209(10), pp. 1334–1347, 2022. https://doi.org/10.1080/00986445.2021.1966423

[25] Song, B., Chen, M., Zhao, L., Qiu, H., Cao, X. "Physicochemical property and colloidal stability of micron- and nano-particle biochar derived from a variety of feedstock sources", Science of The Total Environment, 661, pp. 685–695, 2019. https://doi.org/10.1016/j.scitotenv.2019.01.193

[26] Kumar, A., Luxmi, V. "Development of an efficient eco-friendly photo-catalyst using agro-waste turmeric leaves and its characterizations", Optik, 242, 167057, 2021. https://doi.org/10.1016/j.ijleo.2021.167057

[27] Karimi, F., Zare, N., Jahanshahi, R., Arabpoor, Z., Ayati, A., Krivoshapkin, P., Darabi, R., …, Karimi-Maleh, H. "Natural waste-derived nano photocatalysts for azo dye degradation", Environmental Research, 117202, 2023. https://doi.org/10.1016/j.envres.2023.117202

[28] Erdemoğlu, S., Aksu, S. K., Sayılkan, F., İzgi, B., Asiltürk, M., Sayılkan, H., Frimmel, F., Güçer, Ş. "Photocatalytic degradation of Congo Red by hydrothermally synthesized nanocrystalline TiO_2 and identification of degradation products by LC–MS", Journal of Hazardous Materials, 155(3), pp. 469–476, 2008. https://doi.org/10.1016/j.jhazmat.2007.11.087

[29] Virgin Jeba, S., Sebastiammal, S., Sonia, S., Lesly Fathima, A. "Synthesis, growth mechanism and photocatalytic properties of nickel oxide (NiO) nanoflower: a hydrothermal process", Inorganic and Nano-Metal Chemistry, 51(10), pp. 1431–1441, 2021. https://doi.org/10.1080/24701556.2020.1837163

[30] Chi, W., Yu, F., Dong, G., Bai, L., Guo, D., Chai, D.-F., Zhao, M., Li, J., Zhang, W. "Improved photocatalytic property of ZnO by simultaneously integrating with Ag_3VO_4 for constructing a heterojunction and biochar as charge transfer bridge via microwave hydrothermal method", Journal of Environmental Chemical Engineering, 12(4), 113201, 2024. https://doi.org/10.1016/j.jece.2024.113201

[31] Sneha, Y., Yashas, S. R., Thinley, T., Prabagar Jijoe, S., Puttaiah Shivaraju, H. "Photocatalytic degradation of lomefloxacin antibiotics using hydrothermally synthesized magnesium titanate under visible light-driven energy sources", Environmental Science and Pollution Research, 29(45), pp. 67969–67980, 2022. https://doi.org/10.1007/s11356-022-20540-3

[32] Peng, X., Wang, M., Hu, F., Qiu, F., Dai, H., Cao, Z. "Facile fabrication of hollow biochar carbon-doped TiO_2/CuO composites for the photocatalytic degradation of ammonia nitrogen from aqueous solution", Journal of Alloys and Compounds, 770, pp. 1055–1063, 2019. https://doi.org/10.1016/j.jallcom.2018.08.207

[33] Dahlem Júnior, M. A., Borsoi, C., Hansen, B., Catto, A. L. "Evaluation of different methods for extraction of nanocellulose from yerba mate residues", Carbohydrate Polymers, 218, pp. 78–86, 2019. https://doi.org/10.1016/j.carbpol.2019.04.064

[34] Zazycki, M. A., Godinho, M., Perondi, D., Foletto, E. L., Collazzo, G. C., Dotto, G. L. "New biochar from pecan nutshells as an alternative adsorbent for removing reactive red 141 from aqueous solutions", Journal of Cleaner Production, 171, pp. 57–65, 2018. https://doi.org/10.1016/j.jclepro.2017.10.007

[35] Lazarotto, J. S., de Lima Brombilla, V., Silvestri, S., Foletto, E. L. "Conversion of spent coffee grounds to biochar as promising TiO_2 support for effective degradation of diclofenac in water", Applied Organometallic Chemistry, 34(12), e6001, 2020. https://doi.org/10.1002/aoc.6001

[36] Yukhymchuk, A., Zhukova, D., Prybora, N., Stolyarchuk, N., Bondarchuk, O., Bodnár Yankovych, H., Melnyk, I. V. "Waste-to-Wealth: Unlocking the Potential of Pine Sawdust Biochar for Adsorption of Cobalt(II) and Nickel(II) Ions and Sustainable Elimination of Carbamazepine from Aqueous Solutions", ACS ES&T Water, 4(9), pp. 3943–3955, 2024. https://doi.org/10.1021/acsestwater.4c00241

[37] Uthiravel, V., Narayanamurthi, K., Raja, V., Anandhabasker, S., Kuppusamy, K. "Green synthesis and characterization of TiO_2 and Ag-doped TiO_2 nanoparticles for photocatalytic and antimicrobial applications", Inorganic Chemistry Communications, 170, 113327, 2024. https://doi.org/10.1016/j.inoche.2024.113327

[38] Kumar, A., Luxmi, V. "Effect of calcinations on structural, optical and photocatalytic properties of a green photo-catalyst 'turmeric roots powder'", Optik, 216, 164804, 2020. https://doi.org/10.1016/j.ijleo.2020.164804

[39] Ali, W., Ullah, H., Zada, A., Alamgir, M. K., Muhammad, W., Ahmad, M. J., Nadhman, A. "Effect of calcination temperature on the photoactivities of ZnO/SnO_2 nanocomposites for the degradation of methyl orange", Materials Chemistry and Physics, 213, pp. 259–266, 2018. https://doi.org/10.1016/j.matchemphys.2018.04.015

[40] Zha, D.-W., Li, L.-F., Pan, Y.-X., He, J.-B. "Coconut shell carbon nanosheets facilitating electron transfer for highly efficient visible-light-driven photocatalytic hydrogen production from water", International Journal of Hydrogen Energy, 41(39), pp. 17370–17379, 2016. https://doi.org/10.1016/j.ijhydene.2016.07.227

[41] Dey, A. K., Mishra, S. R., Ahmaruzzaman, M. "Solar light–based advanced oxidation processes for degradation of methylene blue dye using novel Zn-modified CeO_2@biochar", Environmental Science and Pollution Research, 30(18), pp. 53887–53903, 2023. https://doi.org/10.1007/s11356-023-26183-2

[42] Lee, C.-G., Javed, H., Zhang, D., Kim, J.-H., Westerhoff, P., Li, Q., Alvarez, P. J. J. "Porous Electrospun Fibers Embedding TiO_2 for Adsorption and Photocatalytic Degradation of Water Pollutants", Environmental Science & Technology, 52(7), pp. 4285–4293, 2018. https://doi.org/10.1021/acs.est.7b06508

[43] Thommes, M., Kaneko, K., Neimark, A. V., Olivier, J. P., Rodriguez-Reinoso, F., Rouquerol, J., Sing, K. S. W. "Physisorption of gases, with special reference to the evaluation of surface area and pore size distribution (IUPAC Technical Report)", Pure and Applied Chemistry, 87(9–10), pp. 1051–1069, 2015.
https://doi.org/10.1515/pac-2014-1117

[44] Gęca, M., Khalil, A. M., Tang, M., Bhakta, A. K., Snoussi, Y., Nowicki, P., Wiśniewska, M., Chehimi, M. M. "Surface Treatment of Biochar—Methods, Surface Analysis and Potential Applications: A Comprehensive Review", Surfaces, 6(2), pp. 179–213, 2023.
https://doi.org/10.3390/surfaces6020013